Accepted to Phys. Fluids 10.1063/5.0145234

Enhancing droplet rebound on superhydrophobic cones

Qingguo Tang (唐庆国),[1] Shihan Xiang (项诗涵),[1] Shiji Lin (林世玑),[1] Yakang Jin (靳亚康),[1,2] Carlo Antonini,[3] and Longquan Chen (陈龙泉)[1,2,a)]

[1]School of Physics, University of Electronic Science and Technology of China, Chengdu 610054, People's Republic of China

[2]Institute of Electronic and Information Engineering of UESTC in Guangdong, Dongguan 523808, People's Republic of China

[3]Department of Materials Science, University of Milano, Bicocca, via R. Cozzi 55, 20125 Milano, Italy

[a)] Author to whom correspondence should be addressed: lqchen@uestc.edu.cn

ABSTRACT

Understanding the underlying hydrodynamics and developing strategies to control bouncing droplets on superhydrophobic surfaces are of fundamental and practical significance. While recent efforts have mainly focused on regulating the contact time of bouncing droplets, less attention was given to manipulating droplet rebound from the perspective of energy optimization, which determines the long-term successive dynamics. Here, we investigate the impact of water droplets on superhydrophobic cones at low Weber numbers, where ideally complete rebounds arise. In sharp contrast to flat superhydrophobic surfaces, an impinging droplet on a cone-shaped superhydrophobic surface undergoes almost inversion-symmetric spreading and retracting processes with prolonged contact time, and more strikingly, it rebounds with a higher restitution coefficient. Such enhanced droplet rebound is beyond the prediction of existing theoretical models, in which the viscous boundary layer is recognized as the dominant channel of energy dissipation and thus an increase in the contact time would result in a lower restitution coefficient; nevertheless, numerical simulations have confirmed the increase of the restitution coefficient. The quantitative energy and flow field analyses of our numerical results reveal that the suppression of the boundary layer in early impact and the weakening of the viscous flow near the moving edge in the subsequent impact phases, which were not

accounted for yet in existing theoretical models, are the causes for the enhancement of droplet rebound on superhydrophobic cones.

NOMENCLATURE

E_i	interfacial energy during droplet impact (J)
E_{i0}	initial interfacial energy (J)
E_k	instantaneous kinetic energy (J)
E_{k-I}	kinetic energy of impinging droplet before impact (J)
E_{k-R}	kinetic energy of impinging droplet after rebound (J)
E_v	accumulated viscous dissipation energy (J)
E_{v-s}	viscous dissipation energy in spreading stage (J)
E_{v-r}	viscous dissipation energy in retraction stage (J)
E_{v-t}	total viscous dissipation energy (J)
ΔE_i	change of the interfacial energy (J)
$\mathbf{F_g}$	gravitational force per unit volume (N/m^3)
$\mathbf{F_{st}}$	surface tension force per unit volume (N/m^3)
$\mathbf{g}$	gravitational acceleration (m/s^2)
h_{gc}	centre of gravity of droplet (m)
h_I	releasing height of impinging droplet (m)
h_{R-m}	maximum height of droplet rebound (m)
$\mathbf{I}$	identity tensor
L_v	characteristic thickness of viscous boundary layer (m)
$\mathbf{n}$	unit normal vector at the interface
p	pressure (Pa)
P_v	viscous dissipation power (J/s)
p_v	viscous dissipation power in a liquid layer with a thickness of the boundary layer (J/s)
R_0	initial radius of droplet (m)
r_c	droplet-surface contact radius (m)
S_C	droplet-surface contact area (m^2)
t	impact time (s)
t_c	contact time (s)
t_r	retraction time (s)
t_s	spreading time (s)
$\mathbf{u}$	velocity vector (m/s)
V_I	impact velocity (m/s)
V_R	rebound velocity (m/s)
We	Weber number $(= \rho V_I^2 R_0/\gamma)$
α	taper angle of tungsten-steel conical drill (°)
β	reinitialization parameter of level-set function
δ_s	Dirac delta function

ϵ	restitution coefficient
ϵ_{sim}	restitution coefficient from numerical simulations
ϵ_{exp}	restitution coefficient from experimental results
Ω_v	characteristic volume of viscous boundary flow (m^3)
ρ	density of fluid (kg/m^3)
ρ_a	density of air (kg/m^3)
ρ_l	density of liquid (kg/m^3)
γ	surface tension of liquid (N/m)
μ	viscosity of fluid ($Pa \cdot s$)
μ_a	viscosity of air ($Pa \cdot s$)
μ_l	viscosity of liquid ($Pa \cdot s$)
τ	characteristic capillary-inertial time (s)
ϕ	level-set function
ε_{ls}	thickness of interface (m)
κ	curvature of interface (m^{-1})

Accepted to Phys. Fluids 10.1063/5.0145234

I. INTRODUCTION

Endowing solid substrates with hydrophobic microstructures can result in the entrapment of small air pockets when they are brought into contact with water,[1-3] leading to the formation of a thin but strong and stable air cushion. This air cushion separates the liquid from the solid, imparting unique superhydrophobic characteristics to solid surfaces.[1, 4, 5] Statically, a sessile droplet would appear with an apparent contact angle greater than $150°$ on such a surface, due to the minimized liquid-solid contact.[4, 6] Dynamically, titling the solid surface by just a few degrees can cause the droplet to overcome the weak adhesion and hence roll off.[5] More strikingly, the powerful ability of the surface to resist liquid impalement can enable an impinging droplet to rebound off after a short period of contact.[7] It is noteworthy that an ideally complete rebound, where the droplet spreads, retracts and eventually leaves the surface as a whole body, is only achievable in low-velocity impacts; if the impact velocity becomes sufficiently high, a small part of the droplet would be ejected upwards via jetting before the droplet takes off.[8-11]

The rebound of impinging droplets on solid surfaces has gained considerable attention in recent years not only because it is a definitive feature of surface superhydrophobicity,[12] but also because of its decisive role in developing new fluid-based techniques, such as printing surface charge for liquid manipulation,[13] harvesting electricity from raindrops,[14, 15] and fabricating fluid microdispensing devices.[8] Specifically, strenuous efforts have been made to regulate the contact time of bouncing droplets, which sets the duration of mass, momentum, and energy transfer occurring on the surface.[16] Since the droplet dynamics is primarily governed by inertia and capillarity,[5, 17] and considerably affected by liquid-solid interaction[1, 18] and internal fluid dissipation,[19-21] existing strategies for controlling droplet rebounds involve tuning the interplay among these terms. Whereas decorating superhydrophobic surfaces with macrotextures[22, 23] and curved architectures[24] can render asymmetric droplet spreading and recoiling with much shorter contact time compared to ordinary rebounds,[7] adding of a small amount of flexible polymers into

the liquid[25, 26] would strengthen both the droplet-surface adhesion and viscous dissipation, thereby prolonging the residence time on the surface or even thoroughly suppressing droplet rebound. In another line of research, the ratio of the kinetic energies after and before impact, known as the restitution coefficient,[27] provides a quantitative measurement of the energy loss during droplet impact.[17, 28] Although this quantity has been broadly used to characterize the dynamic behaviors of bouncing droplets,[16, 29] its hydrodynamic origins and influencing factors have not been adequately resolved. In most practical applications, maximizing the restitution coefficient is preferred, especially in those ones exploiting the bouncing behaviors.[13, 14]

In this work, we investigate the effects of surface geometry on the ideally complete rebound of water droplets on superhydrophobic surfaces at low Weber numbers. Our experimental results show that a liquid droplet can regain more energy after impinging on cone-shaped superhydrophobic surfaces than on flat ones, leading to a significant increase in the restitution coefficient. By reproducing and analyzing the impact process using numerical simulations, we explicitly demonstrate that such rebound enhancement is achieved by compromising the flow redirection effect on the cone-shaped surface architecture, which weakens the viscous boundary flow and thus reduces the energy loss. Our findings shed new light on the hydrodynamics of droplet impact and provide fresh insights and novel strategies for dynamically manipulating liquid droplets on solid surfaces.

II. EXPERIMENTAL AND NUMERICAL METHODS

Fabrication of Superhydrophobic surfaces. Superhydrophobic surfaces were created by coating solid substrates with hydrophobic silica nanoparticles that were dispersed in an organic reagent (Glaco Mirror Coat "Zero" from Soft 99 Co.). Smooth silicon wafers were used to prepare flat superhydrophobic surfaces, while tungsten-steel conical drills with taper angles (α) of 60°, 90°, and 120° were used for superhydrophobic cones. These surfaces were successively cleaned with acetone, isopropanol and ethanol in an ultrasonic bath for 5 min each, and then dried with

nitrogen blowing before being sprayed with a layer of ~2 μm-thick superhydrophobic coating. After curing at 100 ℃ for 15 min, these hydrophobic nanoparticles assembled into a loosely porous layer (as shown in Fig. S1) to achieve excellent water-repellence.[6] The apparent, advancing and receding contact angles of 4 μL water droplets on these surfaces were measured to be $152.0° \pm 1.0°$, $154.0° \pm 1.2°$, and $148.0° \pm 1.0°$, respectively.

Droplet impact experiment. To conduct droplet impact experiments, we released Millipore Synergy water droplets with radii $R_0 \approx 1.1\,\mathrm{mm}$ onto the superhydrophobic surfaces using a syringe pump, as illustrated in Fig. S2. For cone-shaped superhydrophobic surfaces, a two-camera system with orthogonal optical axes was employed to ensure the impact of the droplet at their center. The impact process was recorded at 40000 fps using a high-speed camera (Phantom v2012, Vision Research Inc., USA). The illumination light was provided by a cold light source and a tracing paper was used to enhance the uniformity of illumination. Our study focused on ideally complete rebounds happening at Weber numbers $We = \rho_l V_I^2 R_0/\gamma \lesssim 1.5$ (where V_I is the impact velocity, while ρ_l and γ denote the density and surface tension of the liquid, respectively), above which the well-known Worthington jet would be stimulated, with the ejection of a satellite droplet prior to bouncing off.[8, 9] Each impact test was repeated at least three times, and we analyzed the recorded videos using image processing algorithms in MATLAB (MathWorks Inc., USA).

Numerical simulations. Numerical simulations were carried out to reproduce the impact phenomena observed in the experiments and analyze the underlying hydrodynamics. The simulations were performed using the commercial finite element software COMSOL Multiphysics v5.3a. In each simulation, an axisymmetric water droplet was set to impinge on a flat, impermeable solid surface with ultra-low surface energy in air, and the two-dimensional Navier–Stokes equations were solved under the incompressibility condition in a computational domain of approximately 3 mm × 3 mm, as illustrated in Fig. S3. The solved equations are[30]

$$\rho\frac{\partial \mathbf{u}}{\partial t} + \rho(\mathbf{u}\cdot\boldsymbol{\nabla})\mathbf{u} = \boldsymbol{\nabla}\cdot[-p\mathbf{I} + \mu(\boldsymbol{\nabla}\mathbf{u} + \boldsymbol{\nabla}\mathbf{u}^{T})] + \mathbf{F_g} + \mathbf{F_{st}}, \quad (1)$$

$$\nabla \cdot \mathbf{u} = 0, \tag{2}$$

where ρ denotes the density of the fluid, μ is the viscosity of the fluid, $\mathbf{u}$ is the velocity vector, t is the impact time, p is the pressure, $\mathbf{I}$ is the identity tensor; $\mathbf{F_g} = \rho\mathbf{g}$ is the gravitational force with $\mathbf{g}$ being the gravitational acceleration; $\mathbf{F_{st}} = \gamma\kappa\delta_s\mathbf{n}$ represents the surface tension force per unit volume, where κ denotes the curvature of the interface, δ_s denotes the Dirac delta function which is non-zero only on the interface, and $\mathbf{n}$ is the unit normal vector at the interface. The surface of the impinging droplet was defined by the level-set function ϕ, which has a value between 0 to 1, with $\phi > 0.5$ representing the liquid phase and $\phi < 0.5$ denoting the air phase. Its motion is described by a convection equation[31, 32]

$$\frac{\partial \phi}{\partial t} + \mathbf{u} \cdot \nabla\phi = \beta\nabla \cdot \phi\left[\varepsilon_{ls}\nabla\phi - \phi(1-\phi)\frac{\nabla\phi}{|\nabla\phi|}\right], \tag{3}$$

where β represents the reinitialization parameter of the level-set function, and it is set to 1, while ε_{ls} defines the thickness of the interface. The fluid density is a function of the level-set function, which is thus given by $\rho = \rho_a + (\rho_l - \rho_a)\phi$, and the fluid viscosity is expressed as $\mu = \mu_a + (\mu_l - \mu_a)\phi$, with ρ_a being the air density, μ_l being the liquid viscosity and μ_a being the air viscosity. The unit normal vector of the interface and its curvature would be determined by $\mathbf{n} = \frac{\nabla\phi}{|\nabla\phi|}\Big|_{\phi=0.5}$ and $\kappa = -\nabla \cdot \mathbf{n}$, respectively.[33]

Following the numerical method in previous works,[34-37] the Navier–Stokes equations concerning the surface tension force [i.e. Equations (1)-(2)] were still employed to describe the local fluid flow near the solid wall after droplet touches the solid surface, and the effects of the solid-liquid contact on the impact dynamics were considered by imposing two boundary conditions: i) the dynamic contact angle of the impinging droplet,[34, 36, 38] which can be obtained from the experiments; 2) the slip boundary condition with a slip length of $20\ \mu m$, which is of the same order of magnitude as the value measured in experimental studies.[39] The domain in Fig. S3 was discretized to approximately 270,000 triangular mesh cells, and the mesh size was kept at $6-10\ \mu m$ in the region of $200\ \mu m$ above the solid wall, while the mesh

size of the remaining region was $10-25\ \mu m$ to ensure the reliability of numerical simulations and reduce the computational cost.

III. RESULTS AND DISCUSSION

We first revisit the bouncing behavior of water droplets on flat superhydrophobic surfaces. The representative phenomenon occurring at $We \approx 1.2$ ($V_I \approx 0.28\ m/s$) is shown in **Fig. 1(a)** (Multimedia view). Upon hitting the surface at $t = 0\ ms$, the incoming vertical flow is redirected radially outwards, and droplet spreading begins immediately. The comparison of the trajectory of the droplet gravity center and that of a free-falling body released from the same height in **Fig. 1(c)** implies that, the downward droplet motion during the early spreading is still inertia-dominated, which lasts for $\sim 1.8\ ms$ before decelerating. That is, we have identified a short-time buffering impact due to liquid fluidity and deformability. Here, we assume that impinging droplets are axisymmetric, and thus their center of gravity is calculated as the centroid of the three-dimensional solid formed by rotating the two-dimensional droplet profile about its axis of symmetry, and its distance to the solid surface is denoted as h_{gc}. Moreover, the spreading would be accompanied by the propagation of capillary waves [indicated by the green arrow in **Fig. 1(a)** (Multimedia view)], if the impact Weber number is larger than one.[8, 40] After attaining its maximum lateral extension at $t \approx 3.4\ ms$, the droplet subsequently retracts back under the drive of the capillary force, and eventually lifts off the surface at $\sim 10.6\ ms$. The overall contact time $t_c \approx 10.6\ ms$ is about 2.5 times the characteristic capillary-inertial time $\tau = \sqrt{\rho_l R_0^3/\gamma} \approx 4.3\ ms$, matching well with the theoretical prediction.[7] It should be noted that the retraction time ($\sim 7.2\ ms$) is much longer than the spreading time ($\sim 3.4\ ms$), suggesting that the impact process is inversion-asymmetric.

Previous studies have demonstrated that bending superhydrophobic surfaces to have a positive curvature would result in shorter contact times for bouncing water droplets.[24, 41] For example, on curved superhydrophobic surfaces with millimeter-scale curvature radii, the contact time is reduced by about 40% compared to that on regular flat superhydrophobic surfaces,[24] and the time reduction can be up

to ~80% on superhydrophobic surfaces patterned with lattices of submillimeter-scale conical posts.[22] Given these findings, we consider the impact of water droplets on millimeter-sized tapered superhydrophobic surfaces, and selected snapshots of an impinging droplet on such a cone-shaped superhydrophobic surface with a taper angle $\alpha = 90°$ at We ≈ 1.2 are illustrated in **Fig. 1(b)** (Multimedia view). After touching the sharp tip, the droplet moves down along the cone-shaped architecture as a free-falling body for about 3.6 ms, which is roughly twice the duration of that on a flat superhydrophobic surface, as indicated in **Fig. 1(c)**. Consequently, the droplet expansion in the radially outward direction is dampened, and the time to reach the maximum deformation is postponed to ~8.0 ms. Another interesting observation is that the capillary wave, stimulated by the transient droplet compression upon impact,[40] is almost inhibited [**Fig. 1(b)** (Multimedia view)]. Unlike on the flat superhydrophobic surface, the droplet undergoes a retraction process (~6.7 ms) with a comparable duration as the spreading process (~8.0 ms) on the cone-shaped superhydrophobic surface; however, the overall contact time is prolonged to ~14.7 ms ≈ 3.4τ, which is opposite to that observed on curved surfaces with finite positive curvatures.[24, 41] More strikingly, the final height to which the droplet can rebound is apparently higher on the cone-shaped surface than on the flat surface, as displayed in **Figs. 1(a)–(c)** (Multimedia views).

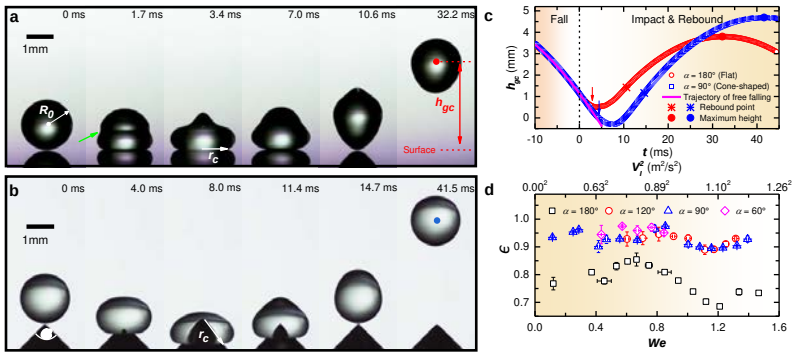

FIG. 1. [(a)-(b)] Selected snapshots of the impact and rebound of a water droplet on a flat superhydrophobic surface ($\alpha = 180°$) and a cone-shaped superhydrophobic

surface with $\alpha = 90°$ at $We \approx 1.2$ ($V_I \approx 0.28\ m/s$), respectively. (c) Temporal evolutions of the center of gravity h_{gc} with respect to the superhydrophobic surface for the impact events in (a) and (b). (d) Plot of the restitution coefficient ϵ as a function of the impact Weber number We for diverse bouncing droplets on the flat and cone-shaped superhydrophobic surfaces. Multimedia views: (a) and (b).

To reveal the effects of surface geometry on the rebound phenomenon in finer details, impact experiments were performed on superhydrophobic surfaces with $\alpha = 60° - 180°$. We adopted the definition of the restitution coefficient in terms of the energy ratio, which directly quantifies the energy recovery or loss in droplet impact. Recognizing that air drag plays a negligible role during the droplet rise after rebound,[17, 18] the restitution coefficient can be expressed and calculated as $\epsilon = E_{k-R}/E_{k-I} = (V_R/V_I)^2 \approx h_{R-m}/h_I$. The results for all bouncing droplets are plotted as a function of the Weber number and the impact velocity in **Fig. 1(d)**. Here E_{k-I} and E_{k-R} are the kinetic energy of the impinging droplet before impact and after rebound, respectively, while h_I and h_{R-m} are the corresponding releasing height and the maximum height of rebound, respectively; V_R denotes the rebound velocity. We find that ϵ of complete rebounds on cone-shaped surfaces is in the range of $90\ \% - 97\ \%$, which is always higher than that on the flat surface (of $70\ \% - 85\ \%$).

The enhancement of droplet rebound on superhydrophobic cones cannot be explained by existing theoretical models in a straightforward manner. In the context of droplet impact dynamics, the energy dissipation in the spreading stage has mainly been attributed to the development of a thin viscous boundary layer above the solid surface,[16, 29] which can be expressed as[20, 42]

$$E_{v-s} = \int_0^{t_s} \int_{\Omega_v} \mu_l \left(\frac{\partial u_i}{\partial x_j} + \frac{\partial u_j}{\partial x_i} \right) \frac{\partial u_i}{\partial x_j} d\Omega dt \approx \mu_l \left(\frac{V_I}{L_v} \right)^2 \Omega_v t_s, \quad (4)$$

where t_s is the total spreading time, $\Omega_v \approx L_v R_0^2$ is the volume of the viscous flow with L_v being the characteristic thickness of the boundary layer. Equation (4) has been successfully employed to describe the spreading dynamics of impinging droplets on diverse wettable surfaces.[16, 29] Though the detailed flow field in the retraction stage

is different from that during spreading, it was shown that the key features of these internal flows, such as the flow structure, the flow velocity, and its duration, have some similarities—at least their characteristic parameters are on the same order of magnitude.[19, 43-45] Therefore, the scaling argument on Eq. (4) is also applicable to estimate the viscous dissipation during droplet retraction on superhydrophobic surfaces,[45] yielding $E_{v-r} \approx \mu_l \left(\frac{V_l}{L_v}\right)^2 \Omega_v t_r$ with t_r being the retraction time. It is worth reminding that the energy loss after rebound—either by air drag or by liquid viscosity—is negligible.[17, 18] Thereby, a simple expression for the restitution coefficient can be obtained from the energy conservation condition, $E_{k-I} = E_{k-R} + E_{v-s} + E_{v-r}$, which reads

$$\epsilon = 1 - \frac{E_{v-s} + E_{v-r}}{E_{k-I}} \approx 1 - \frac{3\mu_l t_c}{2\rho L_v R_0} \quad (5)$$

The equation predicts that an increase in t_c would lead to a decrease in ϵ, whereas in the experiments on superhydrophobic cones, higher restitution coefficients for bouncing droplets with longer contact times were observed [**Fig. 1(d)**].

Accepted to Phys. Fluids 10.1063/5.0145234

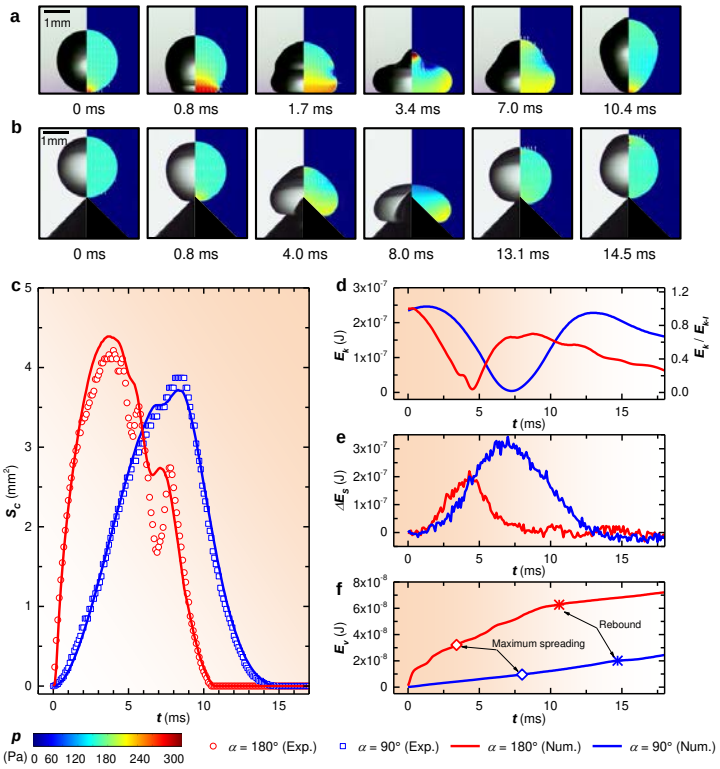

FIG. 2. [(a)-(b)] Comparison of the experimentally observed and numerically simulated droplet configurations for impinging water droplets in **Figs. 1(a)** and **1(b)**. In the right-half images, the hydrodynamic pressure distribution and internal flow fields are also shown. (c) Comparison of the experimental and numerical results of the droplet-surface contact area S_C as a function of impact time t for these two impinging droplets. [(d)-(f)] Plot of the kinetic energy E_k and its proportion with respect to the initial kinetic energy E_k/E_{k-I}, increased interfacial energy ΔE_i, and accumulated viscous dissipation energy E_v as a function of the impact time t. Multimedia views: (a) and (b).

To investigate the hydrodynamics underlying bouncing droplets on superhydrophobic surfaces, finite-element-based numerical simulations were conducted. In brief, we solved the two-dimensional Navier-Stokes equations with a

slip boundary condition[34, 38, 46] and used the level-set method to track the moving liquid-air interface, while imposing the experimentally measured dynamic contact angle of impinging droplets as the other boundary condition in the simulations. More details of the numerical simulation methods are provided in the experimental section. **Figures 2(a)** and **2(b)** (Multimedia views) compare the experimental and numerical results of the droplet shape evolutions for the impact events in **Figs. 1(a)** and **1(b)** (Multimedia views), and the corresponding temporal evolutions of the droplet-surface contact area (S_C) are shown in **Fig. 2(c)**. Note that the droplet-surface contact area was determined using $S_C = \pi r_c^2$ on the flat superhydrophobic surface and $S_C = \pi r_c^2 \sin\frac{\alpha}{2}$ on the superhydrophobic cone, where r_c is the contact radius as defined in **Figs. 1(a)** and **1(b)** (Multimedia views). Obviously, the numerical simulations have fairly well reproduced the dynamic behaviors of these impinging droplets, as both the simulated droplet shape and S_C are in good agreement with the experimental observations.

Based on the numerical results, we first explain the different kinetics of impinging water droplets on flat and cone-shaped superhydrophobic surfaces. When a droplet touches the flat superhydrophobic surface, the transient impact results in remarkable increases in the liquid pressure at the droplet bottom [0 ms in **Fig. 2(a)** (Multimedia view)]. This pressure buildup causes the droplet to quickly spread out, which in turn, generates a viscous force in the liquid and a capillary force along the contact line to counteract spreading. The fast liquid motion near the solid surface also promotes the stimulation of the capillary wave and its subsequent propagation along the droplet surface [$0.8 - 1.7$ ms in **Fig. 2(a)** (Multimedia view)]. The high pressure at the droplet bottom gradually decreases with the ongoing of spreading, while the pressure in the liquid near the droplet edge begins to increase due to the liquid surface tension [$0.8 - 3.4$ ms in **Fig. 2(a)** (Multimedia view)]. After reaching maximum spreading, this capillary pressure drives the droplet to recoil back and eventually to leave the surface [$3.4 - 10.4$ ms in **Fig. 2(a)** (Multimedia view)]. Tilting the superhydrophobic surface considerably lessens the impact force and accordingly the

hydrodynamic pressure at the bottom of the impinging droplet, as shown in the simulation results in **Fig. 2(b)** (Multimedia view), Fig. S4(a) and Fig. S5(a). As a result, instead of quickly spreading radially outwards, the droplet slides down along the cone structure until its kinetic energy is completely transformed. Similar to that on the flat superhydrophobic surface, droplet deformation during spreading leads to a local buildup of capillary pressure in the region of the droplet edge [$0 - 8.0$ ms in **Fig. 2(b)** (Multimedia view)], which later serves as the driving force of droplet retraction and rebound [$8.0 - 14.5$ ms in **Fig. 2(b)** (Multimedia view)].

The simulated droplet shapes and flow fields enable us to quantitatively calculate and evaluate the temporal evolutions of all energy terms involved in the impact process: the kinetic energy E_k, the change of interfacial energy $\Delta E_i = E_i - E_{i0}$, and the accumulated viscous dissipation energy E_v, where E_{i0} and E_i are the initial and dynamic interfacial energies, respectively. As shown in **Figs. 2(d)** and **2(e)**, E_k and ΔE_i exhibit opposite trends during the impact, and their values are in the same broad order of magnitude. More specifically, after contact with the superhydrophobic surface, E_k decreases until the maximum spreading is reached and subsequently increases during droplet recoiling, while ΔE_i first increases and then decreases. By contrast, E_v was found to increase continuously with the impact time and is typically one order of magnitude smaller than E_k and ΔE_i, as illustrated in **Fig. 2(f)**. These findings suggest that the initial kinetic energy of the impinging droplet has been mostly converted into the interfacial energy during droplet spreading, which is subsequently retrieved to promote droplet retraction and rebound, and partially dissipated by liquid viscosity during the whole impact process. It is also observed that the viscous dissipation on the flat superhydrophobic surface is much higher than that on the cone-shaped superhydrophobic surface, particularly in the spreading stage [$t \lesssim 5.0$ ms in **Fig. 2(f)**], where the increase of E_v is more evident. As a consequence, more kinetic energy is stored as the interfacial energy at the maximum spreading on the cone-shaped surface [i.e. $\sim$7.0 ms in **Fig. 2(d)**], driving the droplet to rebound higher [**Fig. 1(c)**]. Moreover, **Fig. 2(f)** also shows that E_v barely increases after the

rebound, indicating that the viscous dissipation mainly occurs during droplet contact with the solid surface. In fact, this finding has been widely presumed in theoretical models for bouncing droplets,[16, 18, 20, 34] whereas our numerical results provide a conclusive validation of such an assumption.

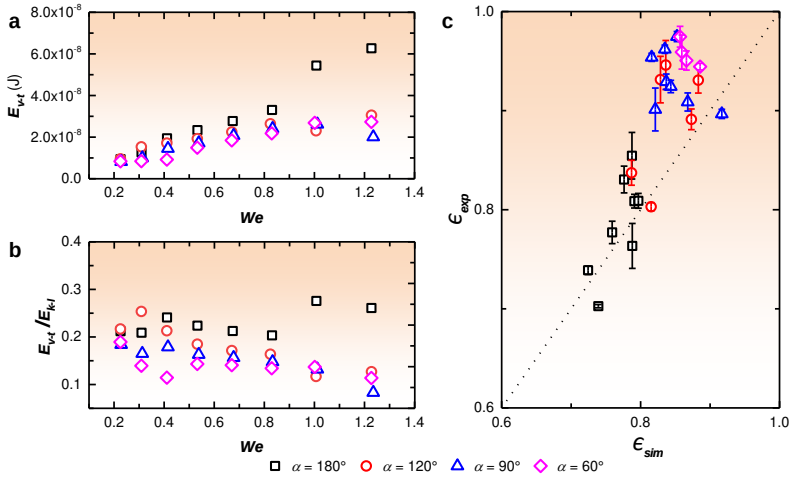

FIG. 3. [(a)-(b)] Accumulated viscous dissipation energy E_{v-t} and its proportion to the kinetic energy of impact E_{v-t}/E_{k-I} as a function of the Weber number We. (c) Comparison of the experimental (ϵ_{exp}) and simulated (ϵ_{sim}) restitution coefficients for all bouncing water droplets. The dashed line denotes $\epsilon_{exp} = \epsilon_{sim}$.

Figure 3(a) shows the total energy loss due to liquid viscosity for diverse impinging droplets until rebound, denoted as E_{v-t}, as a function of We, while the proportion of the total energy loss to the input kinetic energy upon impact, E_{v-t}/E_{k-I}, is summarized in **Fig. 3(b)**. Generally, E_{v-t} increases with increasing We and is typically on the order of 10^{-8} J, occupying approximately $10\,\% - 30\,\%$ of the input kinetic energy. At any given We, the viscous loss of an impinging droplet on the flat superhydrophobic surface is always higher than that on superhydrophobic cones, for which a slight increase with increasing the tapered angle has also been observed. Similarly, E_{v-t}/E_{k-I} is generally higher on the flat surface than on cone-shaped

surfaces; however, it exhibits an overall increasing trend for increasing We on the flat surface, but decreases with increasing We or decreasing α on cone-shaped surfaces. We determined the restitution coefficients for impinging droplets in the numerical simulations using $\epsilon_{sim} = 1 - E_{v-t}/E_{k-I}$, and compared the results with experimental data in **Fig. 3(c)**. Evidently, ϵ_{sim} shows a linearly increasing correlation with ϵ_{exp}, and all data points lie around the straight line $\epsilon_{sim} = \epsilon_{exp}$. The good agreement between the experimental observations and numerical results not only verifies the reliability of our computational method but, more importantly, also confirms that the cone-shaped architecture can effectively alter the energy budgets of impinging droplets and thus regulate their rebound behaviors.

To gain more insight into how surface architecture affects the energy loss in droplet impact, the instantaneous viscous dissipation, or equivalently, the dissipation power, P_v, was calculated. The results for the two representative impacts are displayed in **Figs. 4(a)** and **4(b)** (Multimedia views). Note that the integral of the viscous dissipation power over the contact time would be the total energy dissipation during droplet impact on superhydrophobic surfaces, i.e., $E_{v-t} = \int_0^{t_c} P_v \, dt$. It was found that P_v abruptly increases to a maximum of $\sim 3.7 \times 10^{-5}$ J/s after impact on the flat superhydrophobic surface and then quickly decreases by approximately one order of magnitude to $\sim 7.3 \times 10^{-6}$ J/s, which holds for the remaining time of the dynamics with some fluctuations [**Fig. 4(a)** (Multimedia view)]. By comparison, P_v remains on the order of 10^{-6} J/s throughout the whole impact process on the superhydrophobic cone, as shown in **Fig. 4(b)** (Multimedia view). Similar results were also obtained on superhydrophobic cones with $\alpha = 60°$ and $120°$ [Figs. S4(b) and Fig. S5(b)]. It is thus clear that the difference in energy loss for impinging droplets on the flat and cone-shaped superhydrophobic surfaces stems from the early dynamics of impact.

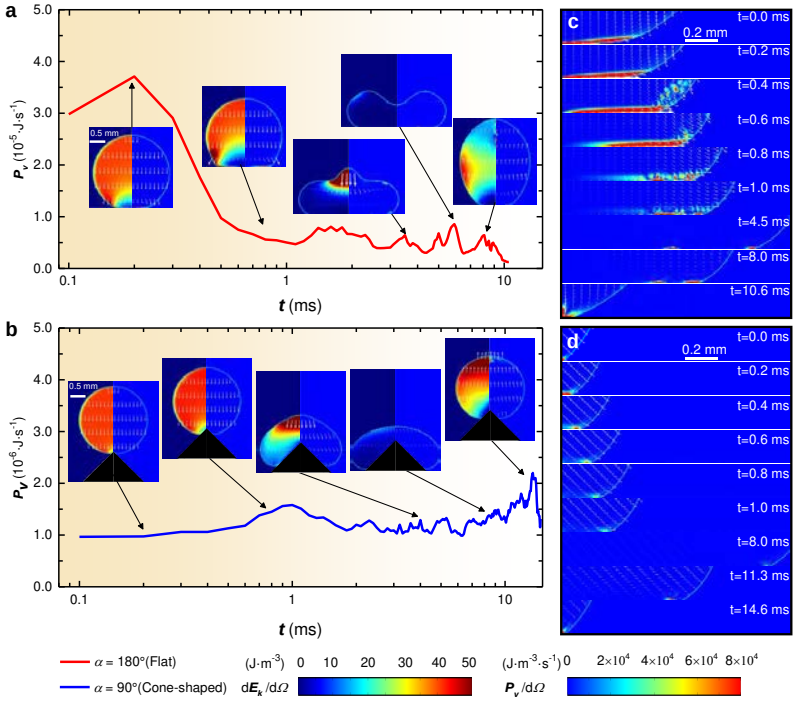

FIG. 4. [(a)-(b)] Temporal evolution of the viscous dissipation power P_v as a function of the impact time t for an impinging droplet on the flat and cone-shaped superhydrophobic surfaces at $We \approx 1.2$, respectively. Insets show spatial distributions of the kinetic energy (left) and viscous dissipation (right) with flow fields (white arrows) at selected impact times. [(c)-(d)] Zoom-in view of the spatial distributions of the viscous dissipation and flow field near the solid surface of impinging droplets in (a) and (b). The tapered surface in (b) was rotated toward the horizontal plane in (d). Multimedia views: (a) and (b).

Two channels of hydrodynamic dissipation have been reported for the impact of liquid droplets on solid surfaces: the viscous dissipation in the boundary layer flow, which has been widely recognized as the dominant one,[16, 20, 29, 34, 42] and the viscous loss due to the propagation of the capillary wave, which was recently considered.[47] By zooming in the boundary region of the impinging droplet on the flat superhydrophobic

surface, we identified the development of a thin shearing layer with a thickness of $L_v \approx 40\ \mu m$ around the impact point in numerical simulations [see $0.2 - 0.6$ ms in **Fig. 4(c)**], due to the redirection of the incoming flow from vertical to horizontal by the solid surface. However, once the kinetic energy of the flow in this layer is completely transferred during spreading, partly into the increased interfacial energy and partly into the viscous dissipation [**Figs. 2(b)** and **2(d)**], a stagnation zone is established, as illustrated in **Fig. 4(c)**. This type of flow field evolution bears a striking similarity to that of impinging liquid jets on solid surfaces.[48] Thereafter, the dissipative region shifts to a small zone near the droplet contact line for the rest of impact, where the shearing flow is much weaker [$0.8 - 10.6$ ms in **Fig. 4(c)**]. By contrast, the redirection of the impinging flow is effectively weakened on the cone-shaped superhydrophobic surface, and the development of a boundary layer with a well-defined thickness around the impact point has been fatally compromised or even inhibited, as shown in **Fig. 4(d)**, Fig. S4(c) and Fig. S5(c). Instead, the weak shearing flow near the moving contact line becomes the main cause of the energy loss in the local region close to the solid surface. On the other hand, when droplets impinge on flat superhydrophobic surfaces at $We \gtrsim 1$, visible capillary wave propagations are observed, as displayed in **Fig. 1(a)** (Multimedia view) and **Fig. 4(a)** (Multimedia view). However, such capillary waves were not observed during droplet impact on superhydrophobic cones [**Fig. 1(b)** (Multimedia view) and **Fig. 4(b)** (Multimedia view)]. These distinct flow characteristics call for an identification of their role in determining the energy budgets of impinging droplets.

Given that the viscous boundary flow is located in a thin layer adjacent to the solid surface, while the stimulated capillary wave would travel from the droplet bottom to its top, we analyzed the spatial distribution of the viscous dissipation power in the direction perpendicular to the solid surface. As illustrated in **Fig. 5(a)**, impinging droplets were decomposed into several liquid layers with heights equal to the thickness of the well-developed boundary layer on the flat superhydrophobic surface L_v, and the viscous dissipation in each layer, p_v, was computed. The sum of

p_v in the entire droplet yields P_v. In **Figs. 5(b)** and **5(d)**, we plot p_v as a function of the distance to the solid surface (i.e., the vertical coordinate of the liquid layer z) for the representative impinging droplets in **Figs. 4(a)** and **4(b)** (Multimedia views) at different impact times. It is seen that at any given time p_v has a value of $10^{-6} - 10^{-5}\,\mathrm{J/s}$ in the region close to the flat superhydrophobic surface [i.e. $6 - 11\%$ of the droplet height H, **Fig. 5(c)**], which is about 1–2 orders of magnitude higher than that in the top region (of $10^{-7}\,\mathrm{J/s}$), wherein the capillary wave travels. This non-uniform energy dissipation is more pronounced in the early spreading at $t \lesssim 0.9$ ms, which exactly corresponds to the buildup of a thin boundary layer [as shown in **Fig. 4(a)** (Multimedia view)], and p_v in the boundary region accounts for more than $80\,\%$ of the total viscous dissipation power in the impinging droplet, i.e., $p_v/P_v > 80\,\%$ as shown in **Fig. 5(b)**. In the further spreading, the viscous flow layer shrinks to a local region around the contact line [**Fig. 4(c)**] and accordingly p_v decreases, but it still plays a dominant role as $p_v/P_v > 60\,\%$. For the impinging droplet on the cone-shaped superhydrophobic surface, where no well-defined boundary layer has been observed, p_v has a value of $10^{-8} - 10^{-7}\,\mathrm{J/s}$, as depicted in **Fig. 5(d)**. Although the viscous dissipation is relatively higher at the bottom ($z/H \lesssim 20\%$) and top ($z/H \gtrsim 75\%$) of the droplet, the maximum p_v/P_v is only $\sim 10\,\%$ [**Fig. 5(e)**]. All of the above analyses suggest that the reduced energy loss and, consequently, the enhanced droplet rebound on superhydrophobic cones are mainly due to the suppression of the formation of the boundary layer and the weakening of the viscous flow near the moving droplet edge, whereas capillary wave propagations and other interfacial distortions of the droplet shape play a minor role in energy dissipation.

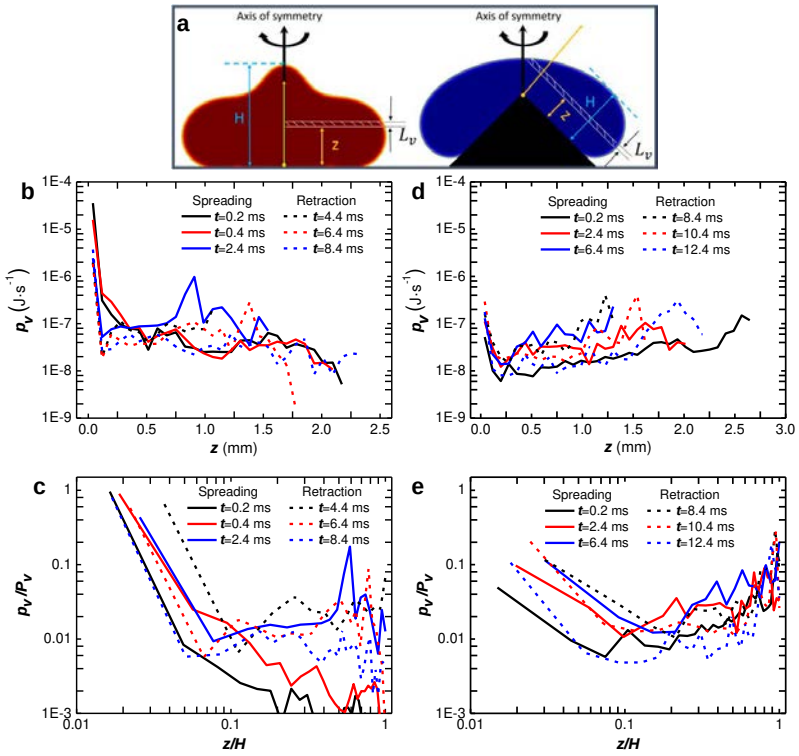

FIG. 5. (a) Illustration of the method to calculate the spatial distribution of the viscous dissipation power p_v in the direction perpendicular to the solid surface. (b) Plot of p_v as a function of the distance to the solid surface z for the impinging droplet on the flat superhydrophobic surface with $We \approx 1.2$ at different impact times. (c) Replot of the data in (b) in the form of p_v/P_v vs. z/H. (d) Plot of p_v as a function of z for the impinging droplet on the cone-shaped superhydrophobic surface with $We \approx 1.2$ at different impact times. (e) Replot of the data in (d) in the form of p_v/P_v vs. z/H.

Looking back at the failure of existing theoretical models to explain the enhancement of droplet rebound on cone-shaped superhydrophobic surfaces, we have also examined the validity of the previous scaling analysis on viscous energy dissipation. It has been generally assumed that a laminar boundary layer with a

well-defined thickness always exists at the droplet-surface contact region,[16, 29] and the corresponding dissipation energy can be derived by integrating the dissipation function in this viscous layer over the timescale of concern (i.e., t_s, t_r or t_c)[20, 26, 42, 45, 49], yielding an expression like Eq. (4). This assumption is partially confirmed in our numerical simulations, where a thin boundary layer with thickness increasing with increasing We [Fig. S6(a)] is established upon impact on the flat superhydrophobic surface [$0 - 0.4$ ms in **Fig. 4(c)**]. However, this boundary layer can only exist for a short period, decreasing with increasing We [Fig. S6(b)], before shrinking to a small region of irregular structure close to the contact line [$0.6 - 4.5$ ms in **Fig. 4(c)**]. Nevertheless, substituting typical experimental values ($\mu_l \approx 10^{-3}$ Pa·s, $V_I \approx 0.28$ m/s, $R_0 \approx 1.1$ mm, $L_v \approx 40$ μm, and $\tau \approx 4.3$ ms) into Eq. (4), we obtained a viscous dissipation energy of the order of 10^{-8} J, consistent with the results of numerical simulations [**Fig. 2(f)**]. Based on these findings, we conclude that although the boundary layer theory cannot precisely describe the flow structure of impinging droplets on flat superhydrophobic surfaces, it does allow for a proper estimation of the energy loss at the magnitude level. By comparison, given the weak effect of the tapered architecture on boundary layer formation, the viscous flow near the moving edge, and the prolongation of contact time, using the same scaling analysis for flat surfaces would reasonably cause overestimation of dissipation energy, and thereby underestimation of the restitution coefficient.

IV. CONCLUSION

In summary, we present a novel strategy for enhancing the rebound of liquid droplets on superhydrophobic surfaces by exploiting sharp cone geometries. In comparison with the dynamic behavior on flat superhydrophobic surfaces,[7-9, 12, 26, 45] an impinging droplet stays longer on cone-shaped superhydrophobic surfaces with tapered angles of $60° - 120°$, and eventually rebounds with a higher coefficient of restitution ($> 90\%$). This nontrivial observation cannot be directly rationalized by the scaling analyses based on the boundary layer theory,[16, 29] which predict that increasing the contact time would lead to a decrease in the restitution coefficient of droplet

rebound. Nonetheless, numerical simulations performed in this study have fairly reproduced all bouncing characteristics of impinging droplets. The coupling analyses of the flow structures and the energy budgets indicate that the promoted rebounds on superhydrophobic cones originate from the suppression of the boundary layer buildup in early impact and the weakening of the viscous flow in the moving edge for the remaining time. This notably lowers the overall energy loss and raise the restitution coefficient. We envision that our findings will provoke broad applications in technological processes where maximizing the contact time and minimizing energy loss are beneficial, such as charge[13] and electricity[14, 15] generation using bouncing droplets.

SUPPLEMENTARY MATERIAL

See the supplementary material for the microscopic structures of superhydrophobic surfaces, the illustration of the experimental setup and the computational domains, and representative numerical simulation results.

AUTHOR CONTRIBUTIONS

L.C. conceived and supervised the research. Q.T. performed experiments and numerical simulations, and analyzed the data. S.X. assisted in part of experiments and S.L. assisted in part of numerical simulations. Q.T., S.L., Y.J., C.A. and L.C. interpreted the data. L.C. and Q.T. wrote the paper with input from all other authors.

ACKNOWLEDGMENTS

This work was supported by the National Natural Science Foundation of China (Grant Nos. 12272085 and 12202096), the Natural Science Foundation of Sichuan Province (Grant Nos. 2023NSFSC0054 and 2022NSFSC1986), and Guangdong Basic and Applied Basic Research Foundation (Grant Nos. 2023A1515010687 and 2021A1515110732).

DATA AVAILABILITY

The data that support the findings of this study are available from the corresponding author (lqchen@uestc.edu.cn) upon reasonable request.

Accepted to Phys. Fluids 10.1063/5.0145234

REFERENCES

[1]D. Quere, "Wetting and roughness," Annu. Rev. Mater. Res. **38**, 71-99 (2008).
[2]K. Rykaczewski, T. Landin, M. L. Walker, J. H. J. Scott and K. K. Varanasi, "Direct Imaging of Complex Nano- to Microscale Interfaces Involving Solid, Liquid, and Gas Phases," ACS Nano **6** (10), 9326-9334 (2012).
[3]B. Y. Zhao, Y. Q. Jia, Y. Xu, E. Bonaccurso, X. Deng, G. K. Auernhammer and L. Q. Chen, "What Can Probing Liquid-Air Menisci Inside Nanopores Teach Us About Macroscopic Wetting Phenomena?," ACS Appl. Mater. Interfaces **13** (5), 6897-6905 (2021).
[4]A. Lafuma and D. Quere, "Superhydrophobic states," Nat. Mater. **2** (7), 457-460 (2003).
[5]D. Quere, "Non-sticking drops," Rep. Prog. Phys. **68** (11), 2495-2532 (2005).
[6]H. J. Butt, C. Semprebon, P. Papadopoulos, D. Vollmer, M. Brinkmann and M. Ciccotti, "Design principles for superamphiphobic surfaces," Soft Matter **9** (2), 418-428 (2013).
[7]D. Richard, C. Clanet and D. Quere, "Surface phenomena - Contact time of a bouncing drop," Nature **417** (6891), 811-811 (2002).
[8]S. J. Lin, D. H. Wang, L. J. Zhang, Y. K. Jin, Z. G. Li, E. Bonaccurso, Z. L. You, X. Deng and L. Q. Chen, "Macrodrop-Impact-Mediated Fluid Microdispensing," Adv. Sci. **8** (16), 2101331 (2021).
[9]D. Bartolo, C. Josserand and D. Bonn, "Singular jets and bubbles in drop impact," Phys. Rev. Lett. **96** (12), 124501 (2006).
[10]L. Q. Chen, L. Li, Z. G. Li and K. Zhang, "Submillimeter-Sized Bubble Entrapment and a High-Speed Jet Emission during Droplet Impact on Solid Surfaces," Langmuir **33** (29), 7225-7230 (2017).
[11]J. W. Guo, S. Zou, S. J. Lin, B. Y. Zhao, X. Deng and L. Q. Chen, "Oblique droplet impact on superhydrophobic surfaces: Jets and bubbles," Phys. Fluids **32** (12), 122112 (2020).
[12]C. R. Crick and I. P. Parkin, "Water droplet bouncing-a definition for superhydrophobic surfaces," Chem. Commun. **47** (44), 12059-12061 (2011).
[13]Q. Q. Sun, D. H. Wang, Y. N. Li, J. H. Zhang, S. J. Ye, J. X. Cui, L. Q. Chen, Z. K. Wang, H. J. Butt, D. Vollmer and X. Deng, "Surface charge printing for programmed droplet transport," Nat. Mater. **18** (9), 936-941 (2019).
[14]Z. Ma, J. W. Ai, Y. S. Shi, K. Wang and B. Su, "A Superhydrophobic Droplet-Based Magnetoelectric Hybrid System to Generate Electricity and Collect Water Simultaneously," Adv. Mater. **32** (50), 2006839 (2020).
[15]W. H. Xu, H. X. Zheng, Y. Liu, X. F. Zhou, C. Zhang, Y. X. Song, X. Deng, M. Leung, Z. B. Yang, R. X. Xu, Z. L. Wang, X. C. Zeng and Z. K. Wang, "A droplet-based electricity generator with high instantaneous power density," Nature **578** (7795), 392-396 (2020).
[16]C. Josserand and S. T. Thoroddsen, "Drop Impact on a Solid Surface," Annu. Rev. Fluid Mech. **48**, 365-391 (2016).

[17]D. Richard and D. Quere, "Bouncing water drops," Europhys. Lett. **50** (6), 769-775 (2000).
[18]Y. L. Wang, Y. G. Zhao, L. J. Sun, A. A. Mehrizi, S. J. Lin, J. W. Guo and L. Q. Chen, "Successive Rebounds of Impinging Water Droplets on Superhydrophobic Surfaces," Langmuir **38** (12), 3860-3867 (2022).
[19]D. Bartolo, C. Josserand and D. Bonn, "Retraction dynamics of aqueous drops upon impact on non-wetting surfaces," J. Fluid Mech. **545**, 329-338 (2005).
[20]M. PasandidehFard, Y. M. Qiao, S. Chandra and J. Mostaghimi, "Capillary effects during droplet impact on a solid surface," Phys. Fluids **8** (3), 650-659 (1996).
[21]A. Jha, P. Chantelot, C. Clanet and D. Quere, "Viscous bouncing," Soft Matter **16** (31), 7270-7273 (2020).
[22]Y. H. Liu, L. Moevius, X. P. Xu, T. Z. Qian, J. M. Yeomans and Z. K. Wang, "Pancake bouncing on superhydrophobic surfaces," Nat. Phys. **10** (7), 515-519 (2014).
[23]J. C. Bird, R. Dhiman, H. M. Kwon and K. K. Varanasi, "Reducing the contact time of a bouncing drop," Nature **503** (7476), 385-388 (2013).
[24]Y. H. Liu, M. Andrew, J. Li, J. M. Yeomans and Z. K. Wang, "Symmetry breaking in drop bouncing on curved surfaces," Nat. Commun. **6**, 10034 (2015).
[25]V. Bergeron, D. Bonn, J. Y. Martin and L. Vovelle, "Controlling droplet deposition with polymer additives," Nature **405** (6788), 772-775 (2000).
[26]B. Li, S. J. Lin, Y. L. Wang, Q. Z. Yuan, S. W. Joo and L. Q. Chen, "Promoting rebound of impinging viscoelastic droplets on heated superhydrophobic surfaces," New J. Phys. **22** (12), 123001 (2020).
[27]W. Goldsmith, *Impact: The Theory and Physical Behaviour of Colliding Solids*. (Edward Arnold Publishers Ltd., London, 1960).
[28]A. L. Biance, F. Chevy, C. Clanet, G. Lagubeau and D. Quere, "On the elasticity of an inertial liquid shock," J. Fluid Mech. **554**, 47-66 (2006).
[29]A. L. Yarin, "Drop impact dynamics: Splashing, spreading, receding, bouncing," Annu. Rev. Fluid Mech. **38**, 159-192 (2006).
[30]S. Popinet, "Numerical Models of Surface Tension," Annu. Rev. Fluid Mech. **50**, 49-75 (2018).
[31]J. A. Sethian and P. Smereka, "Level set methods for fluid interfaces," Annu. Rev. Fluid Mech. **35**, 341-372 (2003).
[32]M. Sussman, E. Fatemi, P. Smereka and S. Osher, "An improved level set method for incompressible two-phase flows," Comput. Fluids **27** (5-6), 663-680 (1998).
[33]E. Olsson and G. Kreiss, "A conservative level set method for two phase flow," J. Comput. Phys. **210** (1), 225-246 (2005).
[34]J. B. Lee, D. Derome, A. Dolatabadi and J. Carmeliet, "Energy Budget of Liquid Drop Impact at Maximum Spreading: Numerical Simulations and Experiments," Langmuir **32** (5), 1279-1288 (2016).
[35]S. J. Lin, B. Y. Zhao, S. Zou, J. W. Guo, Z. Wei and L. Q. Chen, "Impact of viscous droplets on different wettable surfaces: Impact phenomena, the maximum spreading factor, spreading time and post-impact oscillation," J. Colloid Interface Sci. **516**, 86-97 (2018).

[36]K. Yokoi, D. Vadillo, J. Hinch and I. Hutchings, "Numerical studies of the influence of the dynamic contact angle on a droplet impacting on a dry surface," Physics of Fluids **21** (7) (2009).
[37]S. Mukherjee and J. Abraham, "Investigations of drop impact on dry walls with a lattice-Boltzmann model," Journal of Colloid and Interface Science **312** (2), 341-354 (2007).
[38]S. Lin, Y. Wang, L. Sun, A. A. Mehrizi, Y. Jin and L. Chen, "Experimental and numerical investigations on the spreading dynamics of impinging liquid droplets on diverse wettable surfaces," Int. J. Multiphase Flow **153**, 104135 (2022).
[39]J. P. Rothstein, "Slip on Superhydrophobic Surfaces," Annu. Rev. Fluid Mech. **42**, 89-109 (2010).
[40]Y. Renardy, S. Popinet, L. Duchemin, M. Renardy, S. Zaleski, C. Josserand, M. A. Drumright-Clarke, D. Richard, C. Clanet and D. Quere, "Pyramidal and toroidal water drops after impact on a solid surface," J. Fluid Mech. **484**, 69-83 (2003).
[41]P. Chantelot, A. M. Moqaddam, A. Gauthier, S. S. Chikatamarla, C. Clanet, I. V. Karlin and D. Quere, "Water ring-bouncing on repellent singularities," Soft Matter **14** (12), 2227-2233 (2018).
[42]S. Chandra and C. T. Avedisian, "On the collision of a droplet with a solid surface," Proc. R. Soc. A: Math. Phys. Eng. Sci. **432** (1884), 13-41 (1991).
[43]B. Sarma, A. Dalal and D. N. Basu, "Interfacial dynamics of viscous droplets impacting a superhydrophobic candle soot surface: Overview and comparison," Phys. Fluids **34** (1), 012121 (2022).
[44]C. L. Hao, J. Li, Y. Liu, X. F. Zhou, Y. H. Liu, R. Liu, L. F. Che, W. Z. Zhou, D. Sun, L. Li, L. Xu and Z. K. Wang, "Superhydrophobic-like tunable droplet bouncing on slippery liquid interfaces," Nat. Commun. **6**, 7986 (2015).
[45]B. Y. Zhao, X. Wang, K. Zhang, L. Q. Chen and X. Deng, "Impact of Viscous Droplets on Superamphiphobic Surfaces," Langmuir **33** (1), 144-151 (2017).
[46]J. W. Guo, S. J. Lin, B. Y. Zhao, X. Deng and L. Q. Chen, "Spreading of impinging droplets on nanostructured superhydrophobic surfaces," Appl. Phys. Lett. **113** (7), 071602 (2018).
[47]I. Yoon, J. Chergui, D. Juric and S. Shin, "Energetics of spreading droplets and role of capillary waves at low Weber numbers below 10," Phys. Fluids **35** (2), 022104 (2023).
[48]J. Eggers and E. Villermaux, "Physics of liquid jets," Rep. Prog. Phys. **71** (3), 036601 (2008).
[49]C. Ukiwe and D. Y. Kwok, "On the maximum spreading diameter of impacting droplets on well-prepared solid surfaces," Langmuir **21** (2), 666-673 (2005).

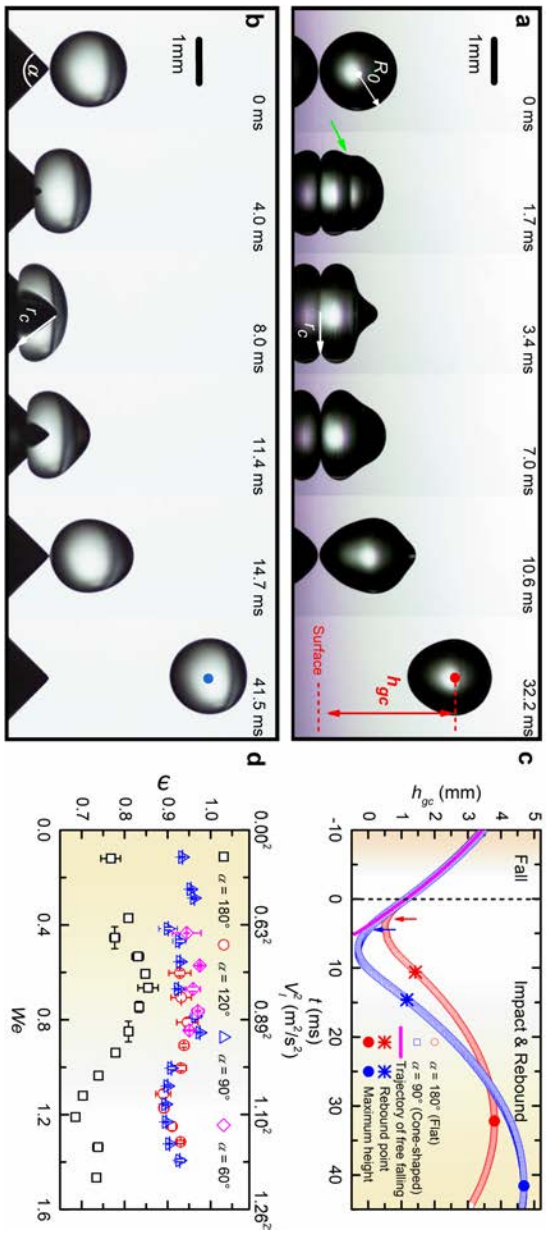

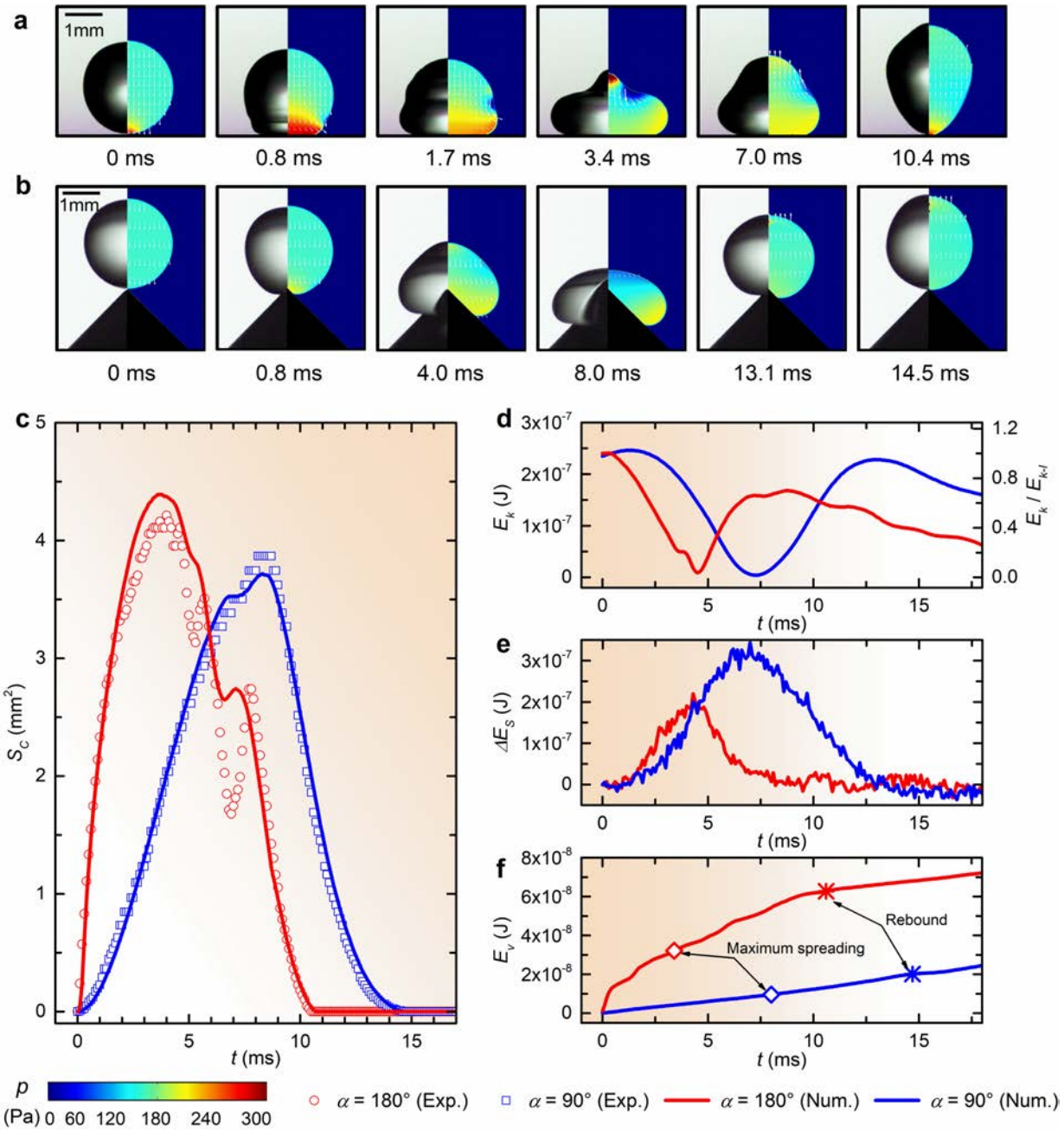

Physics of Fluids

PLEASE CITE THIS ARTICLE AS DOI: 10.1063/5.0145234

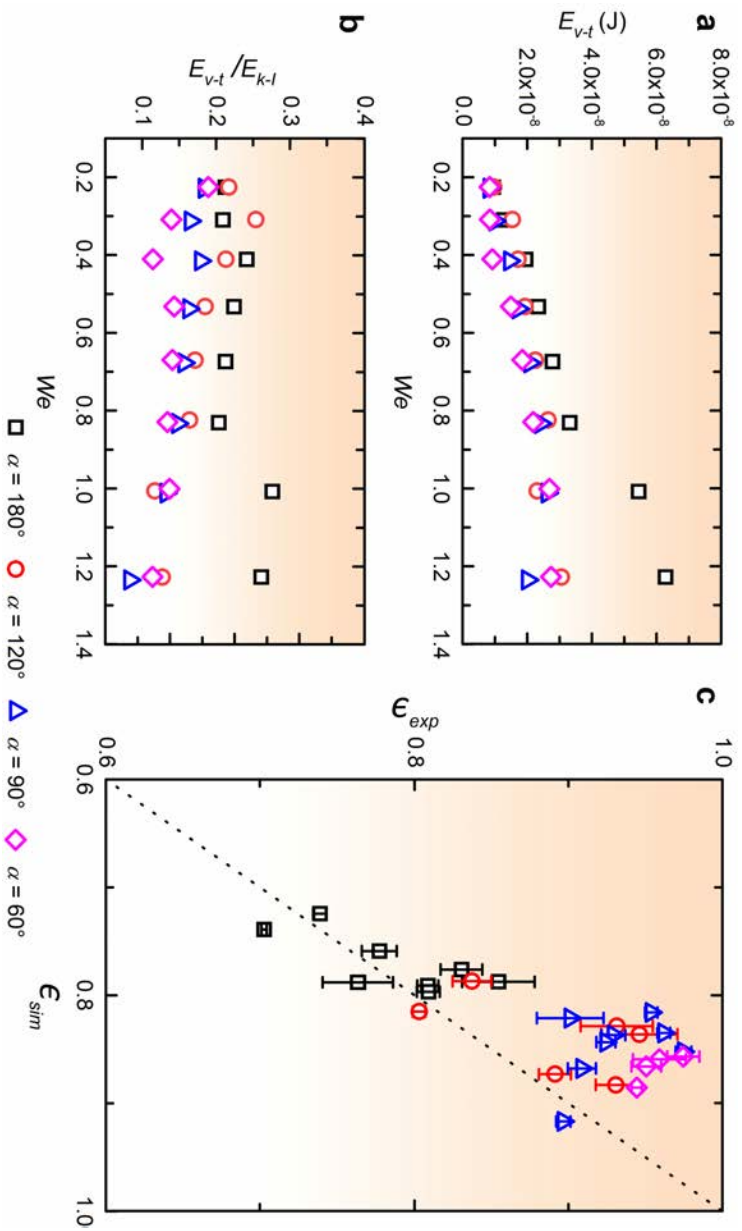

PLEASE CITE THIS ARTICLE AS DOI: 10.1063/5.0145234